

High latitude convection based on long-term incoherent scatter radar observations in North America

Shun-Rong Zhang^{a,*}, John M. Holt^a, Mary McCready^b

^aMIT Haystack Observatory, Westford, MA, USA

^bSRI International, Menlo Park, CA, USA

Received 30 May 2006; received in revised form 11 July 2006; accepted 31 August 2006

Available online 30 March 2007

Abstract

High latitude ionospheric convection patterns and models are obtained based on a composite analysis of incoherent scatter radar (ISR) observations in the North America sector at Millstone Hill and Sondrestrom (MHS). These observations span a combined latitude range of $55^\circ \leq A \leq 82^\circ$ over time periods starting from 1978 for Millstone Hill and from 1995 for Sondrestrom. These models, regional to the America sector, represent average and steady patterns of the convection as driven by the interplanetary magnetic field (IMF) By and Bz or by Kp and the By direction, and update the existing MHS models. This paper describes the ISR and IMF data processing and modeling technique and discusses convection changes under a variety of conditions. In particular, we have examined By and Bz effects on the electrostatic potential at dawn and dusk, the location of the cells, and the shape of the cells; we also present the convection change in response to magnetic activity. This long-term data set has enabled us to study seasonal variations of the convection. The cross polar cap potential is on average higher in equinox than in solstice. With the advance of season from winter to summer, the convection cells appear to move antisunward, and the axis across the two cells rotates toward earlier local times; meanwhile, for By negative, the crescent-shaped dawn cell and circular dusk cell become well defined with a reduced cross polar cap potential, while for By positive, the cross polar cap potential tends to be higher. The dusk–dawn cell similarity in summer is found to be high for By negative and low for By positive, supportive of the theory of lobe cell generation in summer. Because of the asymmetry of the convection response to By negative and positive, and of seasonal differences in the convection, it is speculated that there exist perceptible hemispheric differences in the cross polar cap potential drop.

© 2007 Elsevier Ltd. All rights reserved.

Keywords: Ionospheric convection; Ionospheric model; Magnetosphere–ionosphere coupling; Incoherent scatter radar

1. Introduction

Large-scale magnetospheric electric fields result from interactions between the solar wind and embedded interplanetary magnetic field (IMF) and the Earth's geomagnetic field. Mapping along the magnetic field lines into the ionosphere, they produce high latitude ionospheric plasma convection through the $\mathbf{E} \times \mathbf{B}$ drift and can be a significant

*Corresponding author. Tel.: +1 781 981 5725;

fax: +1 781 981 5766.

E-mail address: shunrong@haystack.mit.edu (S.-R. Zhang).

URL: <http://madrigal.haystack.mit.edu/models/>
(S.-R. Zhang).

source of momentum and energy for the thermosphere. Studying and modeling the high latitude convection pattern are critically important for various space weather efforts. In particular, empirical models of the high latitude convection or electrostatic potential represent a statistical average pattern and have proved to be of great use, although the model results cannot be viewed as a “snapshot” or instantaneous picture of the convection due to its high variability, responding to changes in the IMF, magnetic activity, substorms, and ionospheric conductivity.

Among a variety of convection patterns and models, the following four types are of particular interest. (1) Satellite-based models make use of *in situ* double-probe voltmeter or ion drift meter data from multiple passes over high latitudes (Heelis et al., 1982; Heppner and Maynard, 1987; Rich and Maynard, 1989; Hairston and Heelis, 1990; Weimer, 1996, 2001; Papitashvili and Rich, 2002). (2) The assimilative mapping of ionospheric electrodynamics (AMIE) technique-based convection pattern incorporates direct measurements of the convection and ground geomagnetic data to form global electric potential patterns (Richmond and Kamide, 1988). Convection patterns can also be derived from solely geomagnetic data (Frii-Christensen et al., 1985; Papitashvili et al., 1994). (3) SuperDARN HF radar networks line-of-sight (LOS) measurements are used to construct high latitude convection patterns. From six years of Goose Bay radar data, Ruohoniemi and Greenwald (1996) developed an empirical model which was then combined with observations to generate real-time snapshots of the convection. A more recent effort by Ruohoniemi and Greenwald (2005) resulted in a new model from the SuperDARN northern hemisphere radars observations during 1998–2002 and is expected to replace its 1996 version. (4) Convection models have been also derived from the incoherent scatter radar (ISR) LOS measurements at Chatanika/Sondrestrom, Millstone Hill, and Tromsø (Foster, 1983; Foster et al., 1986b; Holt et al., 1987; Senior et al., 1990). The present study presents a new convection model based on large ISR observational data sets from Millstone Hill (invariant latitude $A = 56^\circ$) and Sondrestrom ($A = 70^\circ$). In the following sections, we first address the motivation and justification for the present study (Section 2), then we describe the IMF data, velocity data deduction for Millstone Hill and Sondrestrom (MHS) observations and the model development, followed by an overview of the

data (Section 3). The main part of our modeling results, including the By and Bz effects on convection, the Kp dependence, and the seasonal variation of the convection pattern, are given in Section 4. The next section is a summary of this research. The Appendix section describes some details about the MHS convection measurements, and compares our result for the “baseline” conditions of $|B_y| = |B_z| = 0$ with two satellite-based convection models.

2. ISR convection models

A convection model developed by Ruohoniemi and Greenwald (2005) for SuperDARN observations represents the most recent effort in the high latitude electric field modeling initiated in the 1970s. ISRs provide another major source of ground-based direct measurements of the convection, and high latitude convection patterns have been extensively studied with various ISRs since the mid-1970s. Earlier results were obtained from the Chatanika radar over $63^\circ \leq A \leq 68^\circ$ (Horwitz et al., 1978), from the Millstone Hill radar over $60^\circ \leq A \leq 75^\circ$ (Evans et al., 1979), from the EISCAT radar over $70^\circ \leq A \leq 77^\circ$ (van Eyken et al., 1984) and over $61^\circ \leq A \leq 72^\circ$ (Alcayd e et al., 1986), and from the Sondrestrom radar ($69^\circ \leq A \leq 82^\circ$) (de la Beaujardi ere et al., 1986). Combining data from multiple radars, a few coordinated observations revealed more complete high latitude convection patterns (e.g., Heelis et al., 1983; Foster et al., 1989; Holt and van Eyken, 2000).

Various empirical models have been developed. For example, Senior et al. (1990) constructed a Kp-dependent convection model from EISCAT tristatic observations over $61^\circ \leq A \leq 72^\circ$ during June 1984 and November 1987. For our present discussion, however, we focus only on results from the America sector, i.e., Chatanika/Sondrestrom and Millstone Hill models. Foster (1983) reported a Chatanika model for auroral electric fields over $58^\circ \leq A \leq 75^\circ$ based on a data set for nine experiment days in summers in 1978–1980 with moderate disturbed conditions. Oliver et al. (1983) gathered 19 24-h experiments made by the Millstone radar in 1978 spanning $60^\circ \leq A \leq 75^\circ$, and constructed models for three levels of Kp. de la Beaujardi ere et al. (1991) studied seasonal variations of the convection using 5 years of Sondrestrom data. The Millstone Hill model was later substantially improved (Holt et al., 1985, 1987) by including 109 experiments conducted between January 1978 and August 1981.

These experiments were mostly from the radar's steerable antenna azimuth scans, in contrast to those very early two beam experiments, and thus a different modeling technique was applied. An updated model, as reported by Foster (1987), was developed by adding some initial Sondrestrom data. Some unpublished efforts were also made in the 1990s to incorporate new data. These Millstone Hill convection models were parameterized largely by two sets of drivers, IMF By and Bz components or Kp and By. Models reported by Foster et al. (1986a, b) and Foster (1987) were parameterized by hemisphere power index (HPI) (Evans et al., 1987) as well.

The MHS convection model is regional as it includes data solely from a single sector. A satellite data-based model, such as that of Weimer (1996), includes data from many longitude sectors so that features unique to a particular region may be smeared out. For instance, in the America sector, geomagnetic latitudes are about 12° higher than corresponding geographic latitudes due to the offset between the north magnetic and geographic poles in this sector. Therefore, for Millstone Hill which is geographically at mid-latitude, the conductivity is higher than for other locations with a similar magnetic latitude, due to the solar EUV flux. This may have some effects on the electric potential and Joule heating rate. An example of such effects is the UT effects indicated in Ruohoniemi and Greenwald (2005) for IMF By negative conditions. A specific regional model would provide the most appropriate description of the electric fields for this longitude sector. Therefore, the ISR-based results are in local time–latitude coordinates for the America sectors. They do not generate global maps; as regional maps, they can only be viewed as global ones when UT/longitude effects are insignificant.

The SuperDARN radars provide very useful instantaneous high latitude convection patterns based on real-time data and a background statistical model. As compared to the SuperDARN radars, ISRs operate less frequently but have accumulated long-term data sets, e.g., for over 25 years at Millstone Hill, and suffer few limitations on local time coverage, as might be the case in the coherent scatter radar echoes during blackouts (Ruohoniemi and Greenwald, 1997). The use of these large data sets would enable us to characterize the long-term climatology of the convection and electric fields, such as the seasonal variation. Also, Millstone Hill lies near the equatorward boundary of most

convection models, and the capability to probe this boundary is otherwise not as easily achieved and is therefore very important.

Historically, the Millstone Hill model (e.g., Foster et al., 1986b) was used to provide the basis functions for the AMIE technique (Richmond et al., 1988). It was used also as a key high latitude input for the coupled thermosphere ionosphere model (CTIM) (Fuller-Rowell et al., 1996). The updated model being discussed here characterizes observations from both MHS with much more data, as compared to the old model published more than one decade ago, and may help improve the performance of other modeling and data assimilation systems. We will use LOS Doppler ion drift measurements from the Millstone radar and the resolved ion drift velocity from the Sondrestrom radar to determine the north–south and east–west ion drift components as a function of magnetic apex latitude (APLAT), apex local time (APLT), and season under various IMF and magnetic activity conditions. The next section describes convection velocity observations at both sites and modeling methodology.

3. Modeling

Descriptions of the convection velocity observations by the ISRs at MHS are given in the Appendices. Here we discuss the modeling method.

3.1. IMF data

As described later, in order to obtain stable background convection patterns, our data are binned into 1-h intervals; therefore we use the corresponding hourly IMF data which are available from the OMNI system at the National Space Science Data Center. This new data set contains near-Earth IMF data from multiple sources with an hourly resolution spanning the period from November, 1961 (IMP 1 launch) to May, 2003. Corrections for the delay time for the IMF signal to travel from spacecraft to the magnetopause were made by the data provider.

The ionospheric convection response to a change in the IMF is completed after (1) the propagation time for the IMF to reach the magnetopause, (2) the magnetosphere–ionosphere communication time, and (3) the ionospheric convection reconfiguration time. The total response time (communication plus reconfiguration times) is on the order of 15–30 min, shorter than previously estimated (see,

e.g., Hairston and Heelis, 1995; Ridley et al., 1998 and references therein). For our current modeling study, as we attempt to achieve better data statistics, we do hourly binning of both IMF data and velocity measurements; therefore our procedure averages out the details of the convection response. We do not expect that this should cause seriously biased convection patterns since the responses, as discussed above, take place in a relatively short time period of half an hour or less, although some degree of compromise is possible (see, e.g., Tanaka, 2001).

3.2. Methodology

We assume that the convection pattern at high latitudes has a repeatable average state and depends on a number of controlling factors that are to be determined, but which might include the IMF, season, K_p , etc.

The data processing involves three steps. First, vector velocities are resolved using approaches slightly different for MHS. Second, the resolved velocity data are combined and further binned to generate the convection velocity corresponding to appropriate IMF or magnetic activity conditions. Third, the electrostatic potential is calculated by least-squares fitting the resolved velocities. These procedures are largely similar to those described in Holt et al. (1987) with three exceptions: seasonal variations were not well established then due to the limited amount of data; the Sondrestrom data were not included; step two aimed at the further improvement of data statistics was not introduced.

To determine velocities for Millstone Hill, LOS data are binned according to season, apex magnetic local time, apex magnetic latitude, and the IMF and/or magnetic activity drivers. (See Appendix A for Millstone Hill wide coverage experiments for convection measurements.) This means that it is not necessary to calculate individual estimates of the vector velocity from pairs or triplets of LOS velocity measurements; therefore measurements which are not normally well suited for the vector velocity calculation, such as elevation scans, can be included in the determination of the mean drift. Within each bin, the observed LOS velocities with corresponding direction cosine values are combined vectorially, and the two velocity components in directions perpendicular to the magnetic fields are determined from the LOS and direction cosine equation in a least squared sense. This procedure produces the true mean convection velocity. We consider two

separate sets of drivers, Set One with B_y and B_z , and Set Two with magnetic activity index K_p and B_y . The two sets are selected to be consistent with those used for the old Millstone Hill model. The binning intervals are 1 h in time and 1° in latitude. We take days 45–115 to be spring, 116–228 summer, 229–299 autumn, and the remainder winter. Each solstice season has 40 more days than each equinox season. This solstice–equinox difference compensates for relatively fewer data being taken near solstice than near equinox. For Set One drivers the interval is 1 nT in B_y and B_z . For Set Two drivers, we consider three K_p levels: $K_p \leq 2$ (quiet); $2 < K_p \leq 5$ (moderate); $K_p > 5$ (disturbed), and two IMF B_y directions: away (positive) and toward (negative) from dusk.

At latitudes close to Millstone Hill, the calculated N–S components may contain a larger uncertainty since the radar beam is primarily in the E–W direction and contributions of field parallel drifts to the LOS velocity are relatively larger than those of field perpendicular drifts. This situation can be improved by adding data from both north and south, at a cost of reduced latitude resolution, and by including local (zenith) LOS data to account for the effect of parallel drifts (Holt et al., 1987). These improvements should be done especially for case studies of the convection but are not implemented for the present statistical work, where we attempt to maintain a unified latitude resolution. Our procedure with a 1° latitude bin used for LOS data binning and a 3° latitude interval used for the subsequent potential fitting (see step three) may also help improve the result near the radar site.

Resolved velocities for Sondrestrom radar are directly available for each comp-scan experiment (see Appendix B) in the database, and therefore they are simply binned in a fashion similar to the Millstone LOS data.

In the second step, the resolved velocities from both sites are combined, and data for the same bin with overlapping APLATs are averaged. We note that the average difference in longitude between MHS LOS measurements is 21° (or 1.4 h in time). Our analysis uses apex local time APLT (not UT). Under a reasonable assumption that longitudinal differences in the LOS and convection electric fields within this small longitude span are small, we can combine data from the two separated sites and capture regional features for APLT and APLAT variations.

A very fine 1 nT interval for B_y and B_z used in the first step binning to form a resolved velocity

distribution that sometimes does not provide proper statistics for an averaged convection model. This is especially the case for very large B_y and B_z (e.g., >6 nT) which occurred less often than smaller B_y and B_z (<4 nT), as can be seen from the B_y and B_z data histogram shown in Fig. 1. So, we apply additional sorting with a wider B_y and B_z interval. Convection results shown in this paper are for a 2 nT interval when Set One drivers are used, except in two cases (Figs. 4 and 5) where we need superior statistics for the seasonal variation discussion.

In the last step, we estimate electrostatic potentials under the commonly used assumption that the electric field \mathbf{E} can be expressed by the electrostatic potential ϕ , i.e., $\mathbf{E} = -\nabla\phi$. They are obtained by least-squares fitting the electric fields, which are derived through $\mathbf{V} = \mathbf{E} \times \mathbf{B}/B^2$, where the vector velocity \mathbf{V} is obtained in step two. ϕ is expressed as a periodic bi-cubic spline function of APLAT and APLT. The spline has knots distributed at 3 h and 3° intervals. The fit is extended over the polar cap by solving Laplace's equation. The velocity values at

the highest latitude are used as the boundary conditions for solving the equation. Such a fitting procedure has the effect of filtering and smoothing, and was also used in prior studies for creating potentials over Millstone Hill (Holt et al., 1984, 1987; Foster et al., 1986b), EISCAT (Alcayd e et al., 1986) and Sondrestrom (de la Beaujardi ere et al., 1991). Weimer (1995) and Ruohoniemi and Greenwald (2005) used a spherical harmonic expansion. The potential can also be calculated by integration of the electric field under the zero potential assumption for the lowest latitudes (Foster, 1983).

Values of the potential are determined with respect to boundary conditions at the lowest latitude. One of the boundary conditions options is to use a local electric field model from Millstone Hill; this may be implemented in the future when such a model is fully developed. The potential may be also set to zero at the lowest latitude as in Holt et al. (1984). For the present study, however, we opt to free the potential at the boundary in the fitting procedure. Therefore, the absolute value of the potential thus obtained is arbitrary and only the change in it is physically meaningful. However, in order to make direct comparisons between peak potentials on both dawn and dusk sides and for different seasons, we assign, as in de la Beaujardi ere et al. (1991), a value for each potential contour such that the diurnal average of the potential at the lowest latitude is zero.

3.3. Data overview

As noted earlier, the Millstone Hill data are LOS velocity and the Sondrestrom data are resolved vector velocity. While the two radars provide a combined coverage between $APLAT = 55\text{--}82^\circ$, most of the Millstone Hill LOS data are within $APLAT = 60\text{--}70^\circ$ and the Sondrestrom resolved velocity is between $APLAT = 70\text{--}75^\circ$. This data coverage therefore allows for a precision determination of the convection cells, especially, the velocity reversal boundary and the southward part of the cell under most solar-geophysical conditions. There are relatively more data points on the dusk side than on the dawn side. The seasonal histogram of data distribution indicates a similar amount of data for the four seasons (the seasonal difference of data points is within 20%), although the solstice season has slightly more data due to more days considered as mentioned earlier. It is possible that the equinox convection pattern signatures could be introduced

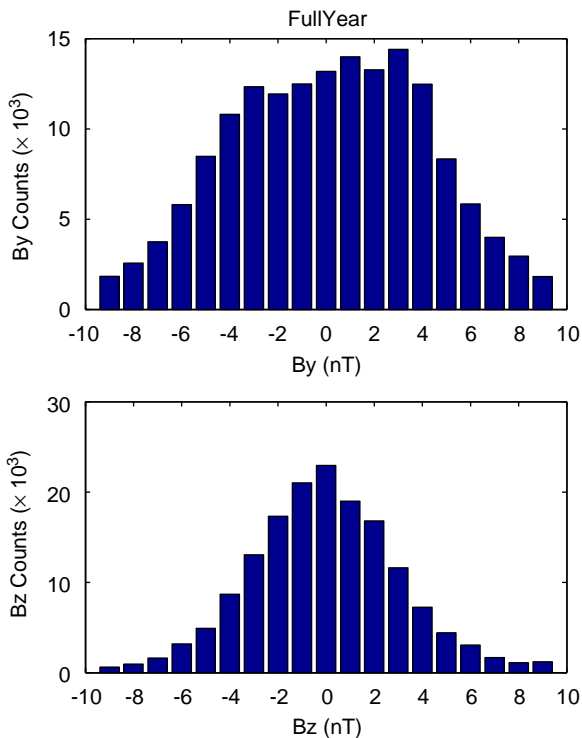


Fig. 1. IMF B_y and B_z data distributions. They include all IMF data from the OMNI database where corresponding line-of-sight data from Millstone Hill radar or resolved velocity data from Sondrestrom radar were available for constructing the convection model.

into the solstice convection pattern, but given the small amount of data from some equinox days and assuming a gradual and smooth variation between equinox and solstice, we expect such a contamination effect should be small; if it does exist, it only results in underestimated seasonal differences. For the three levels of magnetic activity conditions, significant amount of data points are available for disturbed and quiet conditions, but not for moderate magnetic conditions: the number of data points for $K_p \leq 2$ is 0.6 times of that for $K_p > 5$, and is about 9 times of that for $2 < K_p \leq 5$. The IMF B_z histograms shown in Fig. 1 are close to a Gaussian distribution, with the largest data number around 0 nT, but B_z is overall slightly more southward (negative). The IMF B_y component tends to be more positive (away from dusk).

4. Convection patterns and discussions

In this section, we focus on the potential patterns for various IMF conditions and discuss B_y and B_z controls on the convection, as well as the K_p dependency. Special attention will be paid to seasonal variations and effects of the IMF B_y orientation. We will show in this section that the new model is capable of reproducing many known features of the convection and also reveals a few less well-recognized features. Comparisons with other models for the “baseline” conditions are given in Appendix C where we examine the general performance of our model and indicate reasonable agreement between our ISR-based and the satellite-based models.

4.1. B_y and B_z dependency

Fig. 2 shows the electrostatic potential patterns for nine IMF conditions with $B_y = -4, 0, +4$ nT and $B_z = -4, 0, 4$ nT. Shown also are values of potentials at dusk and dawn and across the polar cap. We will use this figure to discuss locations of dawn and dusk cells in the auroral zone, the convection “throat” and cell shape, the polar cap flow orientation, and the Harang discontinuity.

While the duskside cell is generally centered at 1700–1800 APLT, the dawnside cell occurs 1–3 h prior to 0600 APLT. We also see that the location of the cells, especially the dawnside cell, exhibit a seasonal dependence (see Figs. 4 and 5, to be discussed in Section 4.3). It has been suggested that the rotation of the cells (toward earlier local times as

shown here) can be associated with ionospheric conductivity gradients across the auroral zone as well as from night to day in the polar cap (Yasuhara et al., 1983). The rotation has also been considered to be a result of the change of the cell shape (Heelis et al., 1983). Prior studies have shown that the convection velocity vector rotates near local noon and the polar cap flow is alongside the reversal boundary between sunward and antisunward convections (Heelis et al., 1982), forming the convection “throat” near noon and crescent-shaped convection patterns. It was later noted that the cells do not always take on the same crescent-type shape simultaneously on both sides, and the dawn–dusk cell asymmetry features shapes of a crescent type and an approximately circular type (Heelis, 1984).

Our results show clearly the control of the IMF B_y on the cell shape. When $B_y = 0$ nT, the cells are not exactly symmetric, even for $B_z = 0$ nT, with a larger cell and a higher potential on the dusk side. For $B_y > 0$, there is a crescent-shaped dawnside cell and a circular-shaped dusk cell, so that plasma on the duskside flow across local noon into the dawn side in the polar cap. For $B_y < 0$, the dusk cell is more crescent-shaped and larger as compared to the dawn cell, which is more oval-shaped. These features are in quite good agreement with Heelis (1984) results on the dayside convection, and with Weimer (1995).

For a simple two-cell pattern ($B_z \leq 0$), the time of entry of the flow into the polar cap on the dayside determines to a large extent the orientation of the flow across the magnetic pole, indicating details of solar wind and magnetosphere coupling. From the potential contour which runs across the pole, it can be seen that with B_y positive the flow orientation tilts toward the pre-noon and pre-midnight meridian. For B_y negative, however, the flow orientation is almost parallel to the noon–midnight meridian. These results are qualitatively close to Heppner (1977) and Lu et al. (1989).

The B_y dependence of the convection, also known as the Svalgaard–Mansurov effect, has been considered to be a result of asymmetries associated with the reconnection of IMF and geomagnetic field lines at the dayside magnetopause (see a review paper by Smith and Lockwood, 1996). When B_y is positive, due to the magnetic tension the reconnected field lines in the northern hemisphere are pulled toward the dawnside of the polar cap as they are dragged tailward by the magnetosheath flow, causing stronger dawnside convection; when

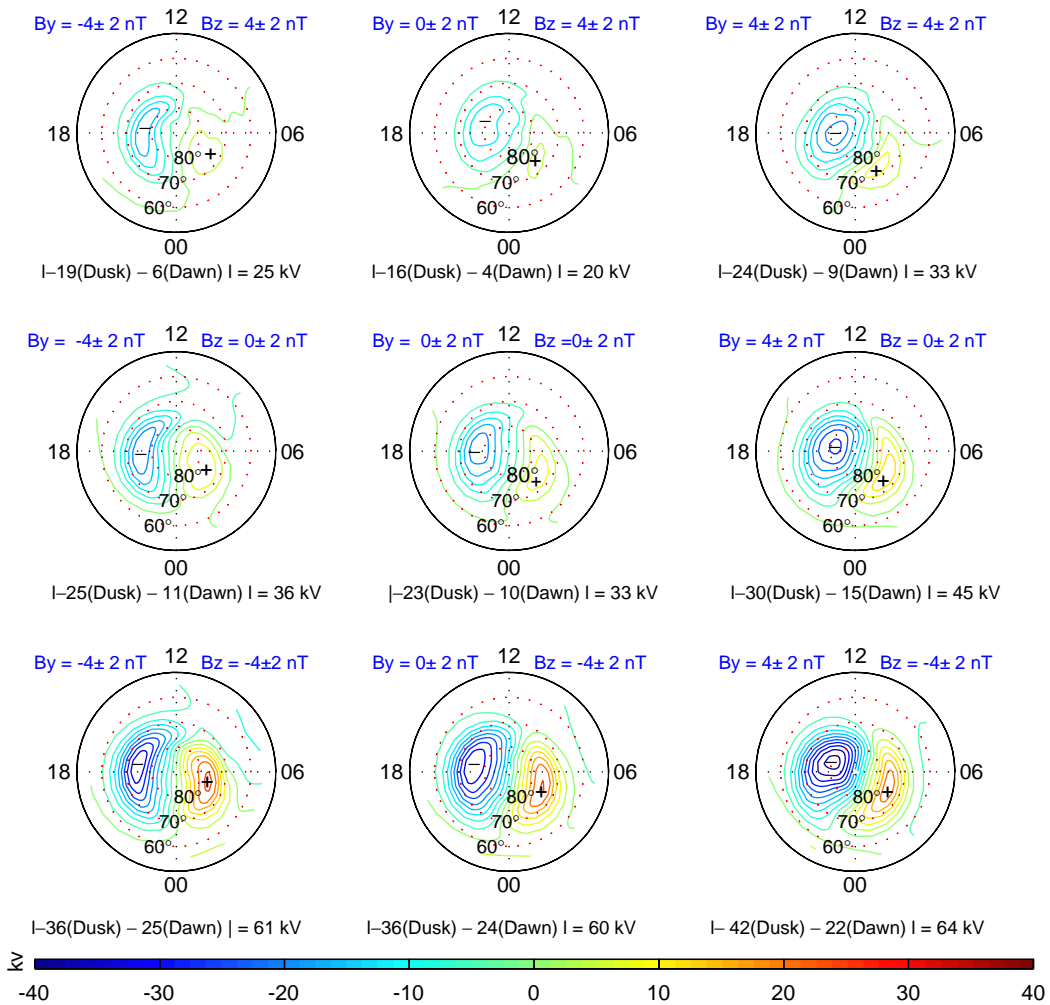


Fig. 2. Millstone Hill/Sondrestrom electrostatic potential annual average patterns driven by IMF B_y ($= -4, 0, 4$ nT) and B_z ($= -4, 0, 4$ nT). Contours are at 4 kV interval between -40 and 40 kV. Given also are dusk and dawn side potentials and the cross polar cap potential ϕ_{pc} .

B_y is negative, they are pulled toward the dusk-side, causing stronger duskside convection. Our results are generally consistent with the reconnection effect, except for large B_z negative cases when the B_y effect is opposite and the magnitude of total velocity at dawn is, at about 400 m/s, not quite symmetric to that at dusk for a large B_y positive, at >400 m/s.

The Harang discontinuity shown in the convection pattern is characterized as the boundary between eastward and westward flows in the auroral convection belt prior to the midnight vortex separation (Heppner, 1977). The sharp boundary often tends to be smoothed out in average models (Oliver et al., 1983; Rich and Hairston, 1994; Ruohoniemi and Greenwald, 1996, 2005). However,

as shown in Fig. 2, our results indicate that the Harang discontinuity appears as a very common feature in almost all conditions without an obvious preference on IMF directions. However, further examination of its Kp dependence (see Fig. 3) indicates that it tends to lie toward lower latitudes with increasing Kp levels, as both cells expand equatorward during high magnetic activity. For moderate activity, the discontinuity boundary appears rather sharp, suggesting a low degree of variability in the Harang discontinuity.

The Harang discontinuity is a pronounced feature during substorm periods. The flow reversal region is associated with the location of substorm onset which has IMF and seasonal effects (Liou et al.,

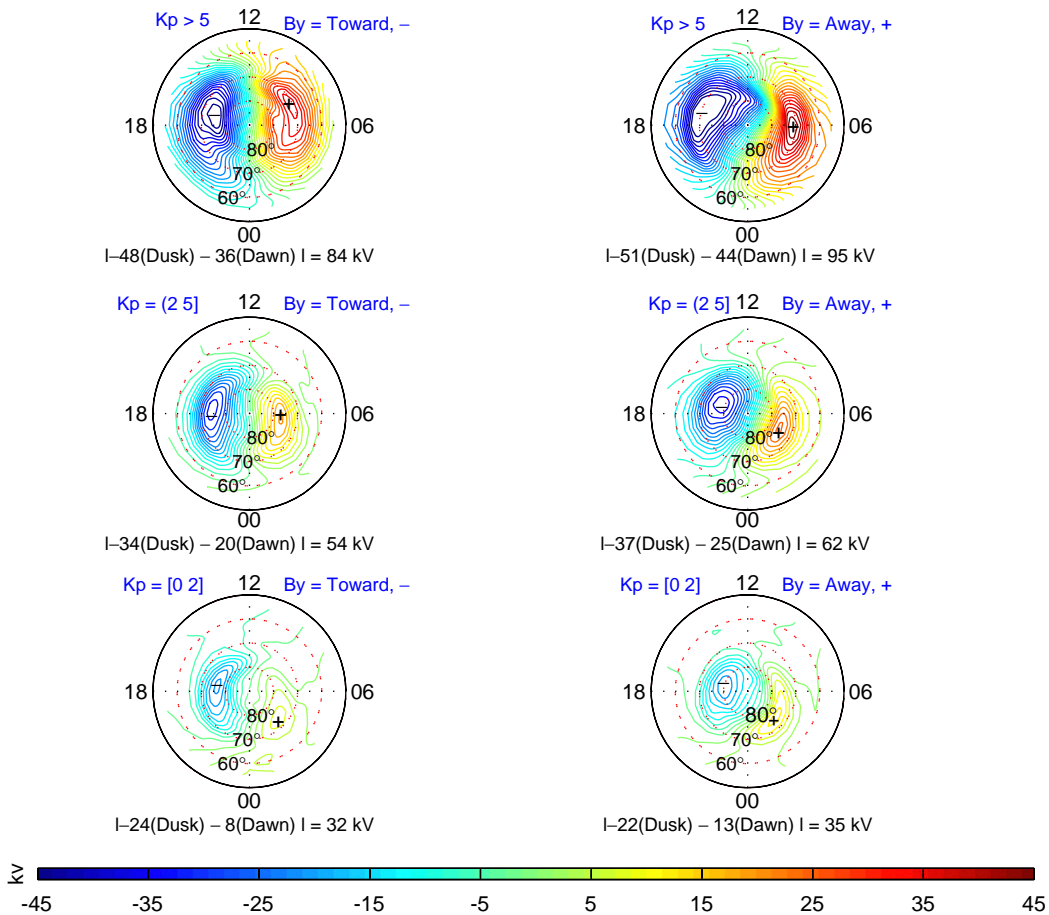


Fig. 3. Same as Fig. 2 but the driving parameters are K_p and B_y direction. Three K_p ranges are selected (see text), and B_y is directed either toward or away from dusk. Different from Fig. 2, contours are at 2.5 kV interval between -45 and 45 kV for better views of the contours at both high and low values. Given also are dusk and dawn side potentials and the cross polar cap potential ϕ_{pc} .

2001). Weimer (1999) and Liang et al. (2006) have characterized the development of the east-to-west flow reversal during the substorm expansion phase. The extension toward post-midnight sectors shown in those prior studies agrees well with the patterns in Fig. 3. The summer-to-winter change of the substorm onset from late evening toward post-midnight is also compatible with corresponding flow reversal changes shown in Figs. 4 and 5 (to be discussed in Section 4.3).

Fig. 2 also indicates that the convection dependence on IMF B_z appears most evident in the quick enhancement of the potential drop as B_z becomes negative. The pattern of the cells does not seem to change significantly for negative B_z . For B_z positive, especially when $|B_z|$ is large, we can see complicated patterns as described in Section 4.4.

4.2. K_p dependence

Sorting the convection according to K_p levels and B_y directions, as was the case in the earlier Millstone Hill model, gives a different view on the convection. The patterns thus obtained, as shown in Fig. 3, are somewhat different from those sorting according to B_y and B_z (Fig. 2) in that the flow in the polar cap has generally a larger dawnward component for the K_p and B_y sorting. However, both sorting results have common features including changes of dawn and dusk cell shapes and of the cross pole cap potential drop in response to the B_y orientation change which are discussed in the last section. In particular, B_y positive tends to give more enhanced cells on both sides than B_y negative, and it produces a higher cross polar cap potential drop ϕ_{pc} than B_y negative does. With increasing K_p , ϕ_{pc}

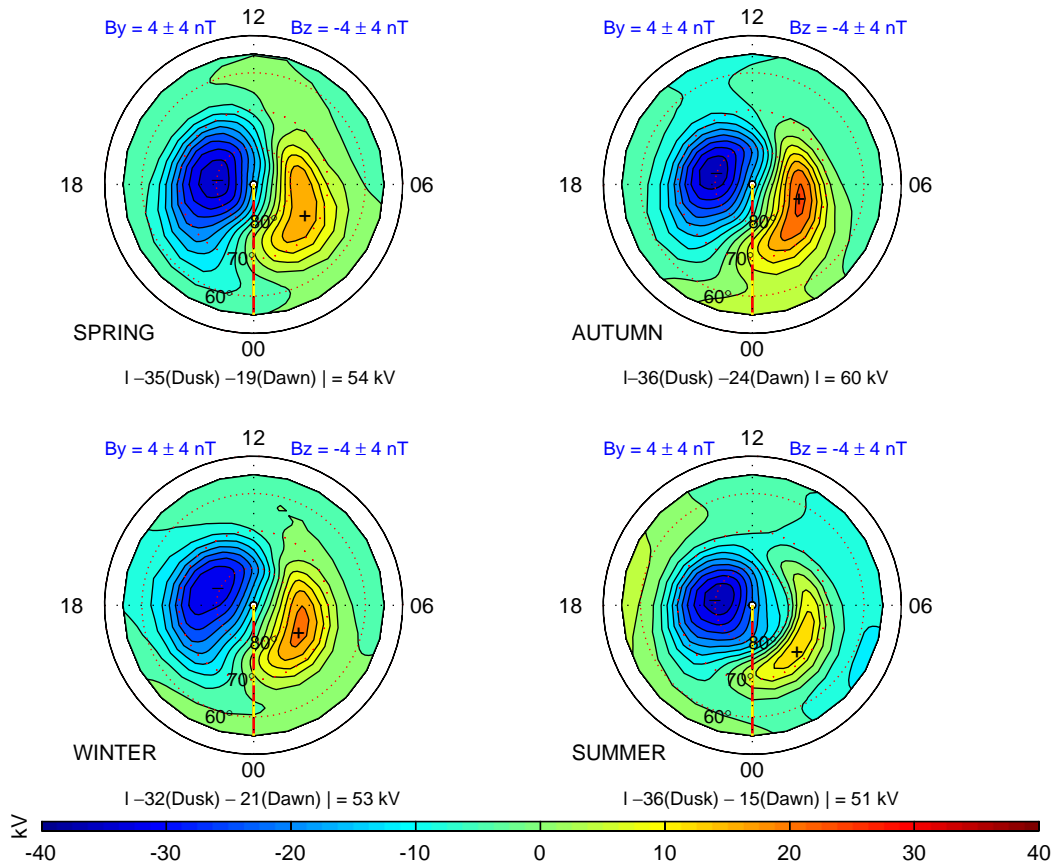


Fig. 4. Electrostatic potential patterns driven by B_y and B_z for four seasons. B_y is between 0 and 8 nT and B_z between -8 and 0 nT. Contours are at 4 kV interval between -40 and 40 kV. Also given are dusk and dawn side potentials and the cross polar cap potential ϕ_{pc} .

increases and the rate of increase appears higher for B_y positive. In other words, the potential drop is more sensitive to K_p for B_y positive. The potential increase as well as the cell expansion toward lower latitudes take place on both dusk and dawn sides. The cell expansion toward lower latitudes is particularly pronounced during positive B_y . The higher magnetic activity causes the rotation toward later local times of both cells for B_y negative, and the polar cap flow orientation is therefore more closely aligned to the noon–midnight meridian corresponding to a larger antisunward flow component. When B_y is positive, the crescent-shaped dawn cell rotates toward later local times and the polar cap flow orientation is tilted downward toward earlier local times. As discussed earlier, the alternation of the polar cap flow orientation appears to be associated with the relative shape of the two cells. An effect of high K_p is to strengthen the alternation.

4.3. Seasonal dependence

The magnetospheric dynamo is often treated as a voltage generator which is assumed to provide as much field-aligned current as needed to maintain constant convection electric fields. This has been a result of ignoring ionospheric dynamo effects (Kamide and Vickrey, 1983). However, there are reasons to expect seasonal variations of the high latitude electric field; to name a few: the ionospheric conductivity gradient as caused by the day–night difference of the solar photoionization (e.g., Wolf, 1970; Atkinson and Hutchison, 1978), the ionospheric conductivity gradient across the auroral zone (Yasuhara et al., 1983), the change of the relative strength of the region I and II field-aligned currents (Nopper and Carovillano, 1979), and the change of the tilt between the magnetic pole axis and the Sun–Earth line, which modifies the projection of IMF on GSM coordinates (de la Beaujardiére et al.,

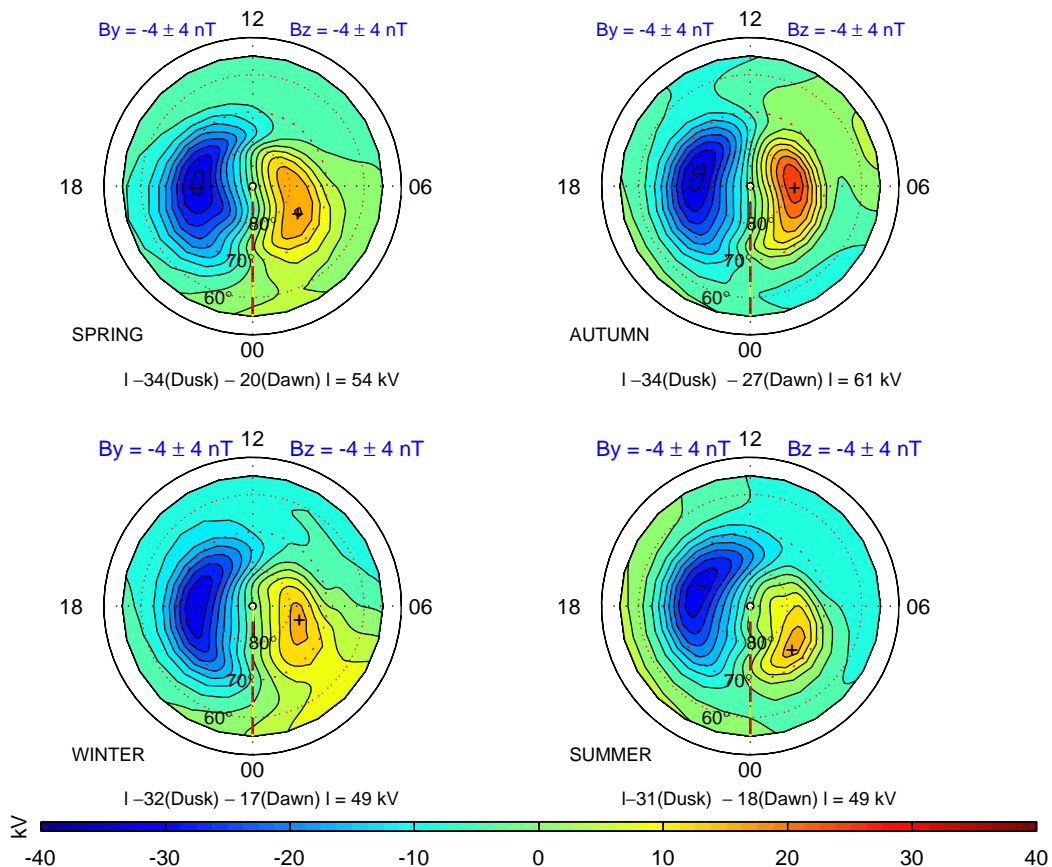


Fig. 5. Electrostatic potential patterns driven by B_y and B_z for four seasons. Both B_y and B_z are between -8 and 0 nT. Contours are at 4 kV interval between -40 and 40 kV. Given also are dusk and dawn side potentials and the cross polar cap potential ϕ_{pc} .

1991). Crooker and Rich (1993) suggested summer–winter differences in the potential due to merging of the open field lines in the lobes with the solar wind. Rich and Hairston (1994) and Weimer (1995) have shown signatures of the seasonal variation in the potentials. Ruohoniemi and Greenwald (2005) discussed the reinforcing effects of B_y direction and season on sculpting the convection and potentials. The variability of the electric field is also found to be seasonally dependent (Codrescu et al., 2000; Matsuo et al., 2003).

4.3.1. Equinox–solstice differences

Our results also reveal seasonal changes in the convection. The convection for B_y between 0 and 8 nT (or B_y positive) and B_z between -8 and 0 nT (or B_z negative) which represents a large portion of our observations, is typically a well-defined two-cell pattern. So, a representative pattern for a given season can be obtained by data averaging even over large B_y and B_z ranges, without incurring serious

pattern distortion. Our B_y and B_z bins are ± 4 nT in the next two figures (Figs. 4 and 5). It can be seen (Fig. 4) that ϕ_{pc} is highest in autumn and lowest in summer, and the equinox average ϕ_{pc} is approximately 5 kV higher than the solstice average. The trend of the potential to be slightly higher at equinox than at solstice can also be identified from results for B_y negative between -8 and 0 nT and B_z negative between -8 and 0 nT, as shown in Fig. 5, where ϕ_{pc} in summer and winter is around 49 kV while spring is 54 kV and autumn is 61 kV.

The Ruohoniemi and Greenwald (2005) results indicated a higher potential in equinox for B_y positive between 3 and 5 nT. But for B_y negative between 5 and 10 nT the equinox potential drop is greater than the winter one and less than the summer one; it is not clear from their work whether this situation prevails for all B_y positive conditions. The higher ϕ_{pc} in equinox was also observed by de la Beaujardiére et al. (1991). They included all their data regardless Kp magnitude and IMF direction. It

is well known that there is more magnetic activity at equinox than at solstice. We can roughly evaluate such an effect by sorting the data according to K_p for the equinox seasons. In fact, using $K_p \leq 5$ data, we see the average ϕ_{pc} in spring and autumn remains slightly higher than the average in summer and winter solstice by 2–3 kV (figures not shown here); however, this value is statistically insignificant.

The cell shapes in spring are very similar to those in autumn, although the potential drops are different for the two equinox seasons. However, the cell shapes in winter are significantly different from those in summer. This and other types of winter–summer differences will be addressed in the next two sections.

4.3.2. Winter–summer differences in cell positions

Between winter and summer the convection pattern exhibits different features. de la Beaujardière et al. (1991) reported the antisunward move of the convection pattern and the rotation toward earlier local times of the dawn and dusk cells with advance of season from winter to summer. They interpreted this in terms of the geometry of field lines and the day–night conductivity gradient. The footprint of the last closed field line is more antisunward in summer than in winter, and the convection seen in the radar’s field of view is shifted antisunward from the winter case to the summer case. The better known day–night conductivity gradient effects also play a role. The gradient generates space charging due to the discontinuity of the Hall flow, and the resulting polarization field in an antisunward direction then drives a flow in the dusk-to-dawn direction, generating a squeezed dawn cell and some rotation of the cell position. We note that since the terminator in summer gives a larger daylight (higher conductivity) area with earlier sunrise and later sunset times, the squeezing process on the dawn side may take place at an earlier time and the change of the dusk cell at a later time, yielding a somewhat antisunward shift of the convection pattern.

Our results also reveal this antisunward move and clockwise rotation of the cells. In Fig. 4 for B_y positive, we see, as compared to corresponding cells in winter, the dusk vortex in summer moves toward 1800 APLT from an earlier time, and the dawn vortex in summer moves toward midnight. In Fig. 5 for B_y negative, the dawn cell moves to an earlier local time as the season turns from winter to

summer. It is also the case (figures not shown here) when the convection data are sorted according to K_p . The move on the dawnside seems more obvious than on the duskside as shown in Figs. 4 and 5, therefore the axis across the dusk and dawn vortices rotates generally clockwise while it moves antisunward. The flow geometry in the dayside polar cap changes generally from along the pre-noon and pre-midnight meridian in winter to the noon–midnight meridian in summer.

4.3.3. Winter–summer differences in responding to B_y orientation

As the convection is influenced strongly by B_y , the winter–summer differences depend also on B_y . Rich and Hairston (1994) and Weimer (1995) have indicated that for B_y positive, ϕ_{pc} tends to be lower in summer than in winter, whereas for B_y negative it tends to be higher in summer. These agree generally with our results shown previously but Fig. 6 presents the detailed behavior of ϕ_{pc} vs B_y for the two seasons with B_z being in the range of -3 and 3 nT.

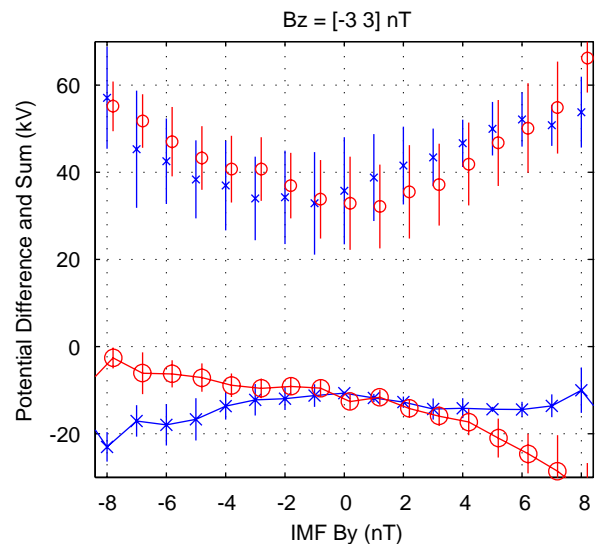


Fig. 6. Cross polar cap potential drops (upper crosses and circles) calculated as the difference between dawn and dusk peak potentials, and the dawn and dusk cell similarity scales (lower curves with markers) calculated as the sum of the two peak potentials as a function of B_y for B_z between -3 and 3 nT for summer (with open circles) and winter (with crosses). The error bars are standard deviations to the averages of potential drops or similarity scales due to B_z values being within ± 3 nT. Crosses and circles are forced to be separated slightly in horizontal direction to avoid overlapping in the error bars.

The winter–summer difference is shown to be round 4 kV on average. The minimum potential drop occurs near $B_y = 1$ nT in summer, whereas it occurs near $B_y = -1$ nT in winter. Therefore, with this 2 nT shift between the winter and the summer curve, the potential drop increases as $|B_y|$ increases, and is asymmetric with respect to the $B_y = 0$ condition for both seasons. Within -8 nT $< |B_y| < 6$ nT the increase in summer is not as large as in winter for B_y positive, and for B_y negative the increase in winter is not as large as in summer. Indeed, as pointed out by Ruohoniemi and Greenwald (2005), B_y positive in summer as well as B_y negative in winter are “reinforcing” B_y sign and season conditions in terms of their effects on the convection and are “associated with reduced values of ϕ_{pc} ”.

Another interesting feature on the winter–summer difference is the pattern asymmetry in the dawn–dusk cells. Figs. 4 and 5 indicate that the nightside cross polar cap antisunward flow inclines toward earlier local times more significantly for B_y positive than negative. In fact for B_y positive, the inclination is stronger in summer than in winter, and the distinctive circular and crescent-shaped cells look better defined with sharper contrast in summer, whereas in winter the cells are more similar and symmetric in shape. For B_y negative, although the dusk cell is more crescent-shaped in both seasons, the dawn and dusk shapes are not as sharply different as for B_y positive.

To evaluate the similarity of the dawn and dusk cell, we define a very simple similarity scale as the sum of dawn (positive) and dusk (negative) potentials. Of course the absolute values of the potentials depend on the lower boundary conditions we have adopted (Section 3.2) and so do the similarity scale values. As long as we keep to the same lower boundary conditions, the similarity scale is meaningful. It indicates the difference between the dusk and dawn potentials but does not give much information about the shape of the cells. This scale is essentially a negative value as the dusk potential value is mostly larger than the dawn one. When this scale is close to 0, the dawn and dusk cell similarity is high.

We can see (Fig. 6, lower curves and markers) that for B_y negative the similarity is higher in summer, and for B_y positive the similarity is lower in summer. This result is supportive of the lobe cell suggestion (Crooker and Rich, 1993). Based on their theory, Crooker and Rich suggested that the two

cells are most equal in the magnitude of the potential in summer for B_y negative but least equal in summer for B_y positive. Weimer (1995) has also given similar results.

4.3.4. Further discussions of seasonal and B_y effects

It is interesting to compare the winter–summer (or spring–autumn) convection with opposite B_y directions. As a result of the reconnection of the IMF and geomagnetic field, the newly opened field line carries a Y component (roughly dawn–dusk direction). For positive IMF B_y the field lines in the northern hemisphere move toward dawn, whereas in the southern hemisphere they move toward dusk. In the ionosphere the flows are eastward or westward, oppositely directed in the two hemispheres (Smith and Lockwood, 1996). In order to obtain, for a given B_y , the convection pattern for southern hemisphere from northern hemisphere results, or combine both hemisphere data to form a single pattern (as in creating satellite data-based convection models), it is widely assumed that the northern hemisphere convection pattern for B_y positive is equivalent to the southern hemisphere one for B_y negative (Heppner and Maynard, 1987; Rich and Hairston, 1994; Weimer, 1995). Case studies by Lu et al. (1994) also indicated that the mirror image assumption was valid for B_z negative. According to this assumption, the convection and ϕ_{pc} in summer hemisphere for B_y positive (ϕ_s^+) are equivalent to the convection and ϕ_{pc} in winter hemisphere for B_y negative (ϕ_w^-), or for the potential drop, $\phi_s^+ \sim \phi_w^-$. Similarly, $\phi_s^- \sim \phi_w^+$, $\phi_S^+ \sim \phi_A^-$, and $\phi_S^- \sim \phi_A^+$, where capitalized S and A stand for spring and autumn and + and – are B_y signs. Our result indicates that the differences of these paired potentials, or “hemispheric” difference, are $|\phi_s^- - \phi_w^+| = 5$ kV, $|\phi_s^+ - \phi_w^-| = 6$ kV, $|\phi_A^- - \phi_S^+| = 7$ kV, and $|\phi_A^+ - \phi_S^-| = 7$ kV for $K_p \leq 5$. This 5–7 kV difference agrees with the de la Beaujardiére et al. (1991) results, although the B_y direction and magnetic activity were not considered there, but our results are considerably stable across the four conditions. “Hemispheric” differences as seen from sorting the data according to B_y with $B_z < 0$ (Figs. 4 and 5) are between 2 and 7 kV, being larger in the equinox.

The above estimate of the “hemispheric” difference is an average over various geophysical conditions. The difference is noticeable although it may not be significant and within the margin of errors. In fact, uncertainty in the estimate could be larger than those indicated in the error bars (of about 10 kV for the potential drop) in Fig. 6 which are due

to changes in B_z between -3 and 3 nT. Additional errors can occur in earlier steps of data processing where the resolved velocity is derived and the potential is fitted. Nevertheless, it should be noted that the above results of the “hemispheric” difference tend to be persistent and stable among different seasons, whether or not the data are sorted by B_y – B_z values or by K_p – B_y direction. Therefore, it seems that such “hemispheric” differences are perceptible and the assumption of mirror images could be questionable for some applications. The procedure to simply switch the B_y sign in order to obtain the convection for the conjugate hemisphere may be not always appropriate. The reasons for that difference lie in, as shown in Fig. 6, the asymmetric convection response to B_y negative and positive and in seasonal differences in the convection.

4.4. IMF B_z positive

We have so far considered two-cell patterns which appear in most of conditions when data are sorted

according to K_p and B_y , or according to B_y and B_z where B_z is negative or at least $|B_z| < 4$ nT. The convection pattern becomes complicated when B_z is positive and large (or according to Lu et al., 1994, $B_z > |B_y|$), and even average patterns can be quite disorganized. Fig. 7 shows an example of a somewhat better organized convection velocity pattern, where we can see clear and persistent sunward flows across the magnetic pole, especially, on the dayside. Note that in our procedure of calculating the potential (and convection) over the polar cap, we solve Laplace’s equation, and velocity values at the highest latitude ($\Lambda = 82^\circ$) are used as boundary conditions for solving the equation. These flows seem more likely part of additional convection cells. In more complicated examples, the sunward flow can be found within the polar cap (but not necessarily running across the pole), near either local noon, dusk and or dawn. For B_z positive, the cross polar cap potential ϕ_{pc} is significantly reduced, and the response of ϕ_{pc} to B_z negative is totally asymmetric to the response to B_z positive.

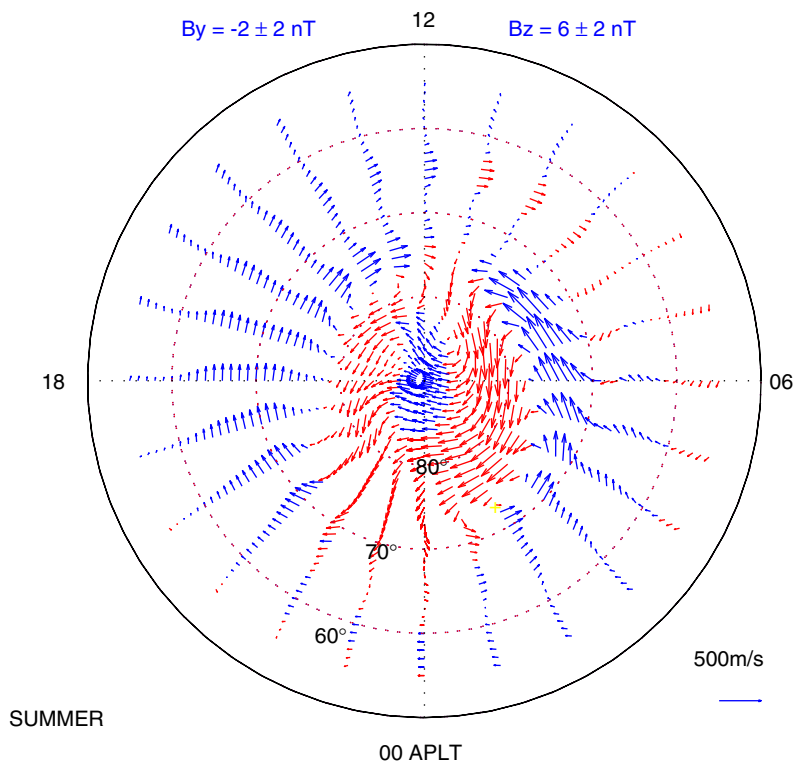


Fig. 7. A sample pattern of the convection velocity for $B_z = 6$ nT and $B_y = -2$ nT in autumn, showing sunward flows in the polar cap. The blue arrows are velocities with sunward components (or dusk-to-dawn electric fields), and the red ones are velocities with antisunward components.

5. Summary

Long-term databases from ISR observations of the high latitude plasma convection in America longitudes at MHS have been used to construct new convection velocity and electrostatic potential models and to study the morphology and IMF controls of the convection. These models represent the average and steady patterns of the electric fields over APLAT $> 55^\circ$ in America sectors. Our models are a significant update to the existing Millstone Hill models, including Millstone Hill data since 1979 and Sondrestrom data since 1995.

Features of the electrostatic potential pattern have been identified from this study and include the variation of locations of dawn and dusk cells in the auroral zone, the convection “throat” and cell shape, the polar cap flow orientation, and the Harang discontinuity. These are largely consistent with some existing empirical models. In particular, the convection cells change their shape between a crescent type and a circular type when B_y changes its orientation and, therefore, the entry of the flow into the polar cap, the “throat” structure, as well as the polar cap flow orientation are affected. For B_y positive there is a circular duskside cell and a crescent dawnside cell, and for B_y negative there is a circular dawnside cell and a crescent duskside cell. The Harang discontinuity signature in the sharp reverse of the flow direction near midnight is seen commonly and not totally smoothed out even in these average models. As a result of the K_p increase, expansion of both dawn and dusk cells is found to appear toward lower latitudes. The K_p effect is stronger for B_y positive than for B_y negative, in terms of the magnitude of increase in the cross polar cap potential ϕ_{pc} and the rotation of the polar cap flow with respect to the noon–midnight meridian.

The seasonal dependence and winter–summer difference of the high latitude convection are also studied. The cross polar cap potential is on average higher in equinox than in solstice. With the advance of season from winter to summer, the convection pattern appears to move antisunward and the dawn–dusk cell axis rotates toward earlier local times. Meanwhile, the cross polar cap potential becomes weaker for B_y positive and tends to be enhanced for B_y negative; therefore the two reinforcing combinations, B_y positive and summer, and B_y negative and winter, give rise to low cross polar cap potentials. Compared to in winter, the dusk–dawn cell similarity in summer is found to be

higher for B_y negative and lower for B_y positive, supportive of the theory of lobe cell generation in summer (Crooker and Rich, 1993). While our results are largely consistent with some earlier studies on the seasonal variation of the convection, they exhibit more detailed evolution of the cell, in particular, the cross polar cap potentials as a function of B_y .

A direct consequence of the seasonal and IMF B_y sign dependence is the discussion of the hemispheric difference in the cross polar cap potential. Our derived “hemispheric” difference can reach up to 7 kV. This value is large enough for us to question the mirror image assumption on the global convection picture. Our modeling result has also shown complicated convection patterns for large positive B_z , and the sunward flow in the polar cap can be seen clearly.

In summary, by using a combined large data set from ISR observations at MHS, we have created a high latitude convection model which is capable of reproducing and quantifying many known features on the electric fields while characterizing some less recognized variations. Our present work, however, has not addressed a few other aspects of the high latitude convection model, such as modules driven by hemispheric power index and the time history effects of IMF B_y and B_z development. These are deserving of future study.

Acknowledgments

We thank the members of the Haystack Observatory Atmospheric Sciences Group and of SRI Sondrestrom Facility, in particular, Bill Rideout and Angela Li, for assembling and maintaining the Madrigal Database containing data from Millstone Hill and Sondrestrom. We thank John Foster for his very valuable comments on the contents and structure of the manuscript. The Millstone Hill incoherent scatter radar is supported by a cooperative agreement between the US National Science Foundation and the Massachusetts Institute of Technology. The Sondrestrom Radar measurements and analysis are supported under cooperative agreement ATM-0334122 between the US National Science Foundation and SRI International. The IMF data were obtained from the OMNI system at National Space Science Data Center. This research was supported by NSF Space Weather Grant ATM-0207748. The HMR89 and the Weimer models were obtained from the CEDAR database.

Appendix A. Millstone Hill wide coverage experiments

Incoherent scatter measurements of convection electric fields became possible from Millstone Hill in 1978 following the acquisition of a 46-m steerable antenna (MISA) that can be used with the UHF radar. Most of the early experiments were carried out by directing the antenna beam alternately 15° east and west of the magnetic meridian to secure measurements of two components of the drift velocity. Elevations of 15° and 4° were employed to cover a complete range of latitudes. An empirical model reported by Oliver et al. (1983) was based on this type of observation. Commencing in 1979, a new observing technique was implemented. In this mode the antenna is moved slowly and continuously either in azimuth or in elevation and, after each MISA scan, observations are switched to the vertically directed 67-m antenna to provide local ionospheric measurements. The MISA scan rates are normally $4\text{--}10^\circ/\text{min}$ in azimuth and $2\text{--}4^\circ/\text{min}$ in elevation for the convection experiments. A long-pulse of about $1280\text{--}2000\ \mu\text{s}$ is often used, yielding an altitude resolution of $35\text{--}80\ \text{km}$ (depending on range) and a spatial resolution of $150\text{--}300\ \text{km}$. The typical integration time is 30 s.

From LOS observations a map of the convection velocity within the radar's field of view can be constructed. This is possible under the assumption that well to the north of Millstone Hill the LOS velocities measured at low elevation angles result primarily from ion drifts perpendicular to the magnetic field. In fact far to the north the radar is sensitive chiefly to N–S drifts, while closer to the observatory the E–W component dominates. See Holt et al. (1987) for more details.

Appendix B. Sondrestrom comp-scan experiments and the resolved velocity

Since about 1995, the Sondrestrom ISR has routinely used an antenna scanning mode that allows the determination of the F-region ion convection over about 12° of latitude. The transmitted pulse scheme allows 48-km range resolution of the LOS returns. The antenna moves in both azimuth and elevation (called a composite scan) and defines a plane that is parallel at any given altitude to the magnetic meridian. This plane is tipped, most commonly 25° from the zenith, alternating to the east and west of the site. Each scan duration is

commonly 4 min. The LOS ion velocities from the same altitudes and latitudes of consecutive scans are combined to resolve the horizontal flow perpendicular to the magnetic field. This technique works well when the parallel drift is minimal, there is longitudinal homogeneity between the east and west scans, and there is temporal stability on the order of some minutes. This technique is discussed in more detail on-line at http://isr.sri.com/instruments/data/is_radar.html.

Appendix C. Comparisons between MHS and other models

Direct comparisons of the new MHS model with other models are not always possible because of different driving parameters adopted for different models. For example, the old MHS model (Foster, 1987) provides patterns for four conditions for all combinations of B_y and B_z orientations while the new one corresponds to discrete B_y and B_z values between -10 and $10\ \text{nT}$ for a given season or as annual averages. In general, however, patterns obtained from the two models appear to be similar, in terms of positions of the two cells, the cell sizes, the flow orientation in the polar cap with respect to the noon–midnight meridian, etc. The Heppner–Maynard–Rich model HMR89 (Rich and Maynard, 1989) gives seasonally averaged patterns for various B_y , B_z , and K_p . The Weimer (1996) model (Weimer96) is driven by more parameters including B_y , B_z , the solar wind speed for any given date of the year (but no seasonally averaged patterns are readily available). Under some assumptions on K_p and the solar wind speed, however, these two models are comparable with our new IMF-dependent ISR convection model.

We compare here the “base-line” potential patterns obtained from the new MHS, HMR89 and Weimer96 models for $B_y = B_z = 0\ \text{nT}$, a condition that occurs very often statistically as mentioned before. Fig. C.1 shows the annual average electric potential pattern obtained from fitting the average electric fields, superposed by the convection velocity calculated from the potentials, as well as potential values on the dawn and dusk sides and across the polar cap. Fig. C.2 presents HMR89 potential patterns for $K_p = 1$. Among various K_p , $K_p = 1$ generates the polar cap potential ϕ_{pc} closest to what is given by the new MHS. (Note, the CGM magnetic latitude and local time coordinates used by the HMR89 and Weimer96 are very close to

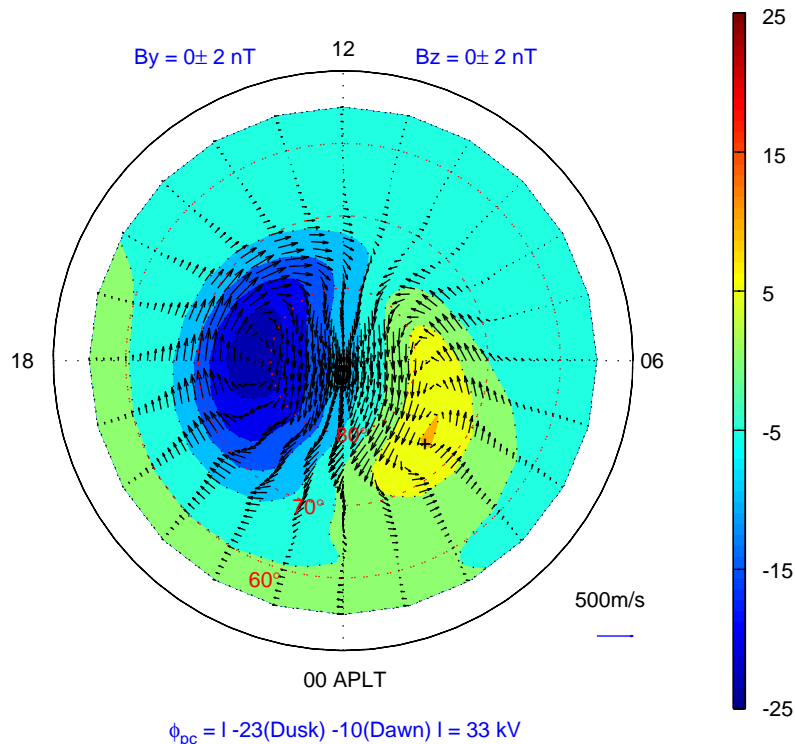


Fig. C.1. A baseline electric potential pattern for $B_y = B_z = 0$ nT as an annual average, overlapped by the convection velocity vector calculated from the potential. Equipotentials are given at 5 kV interval. Dusk and dawn side potentials as well as the cross polar cap potential ϕ_{pc} are also indicated.

the APLAT and local time coordinates used by the MHS models, with latitude differences generally less than 0.5° , and local time differences less than 5 min for East North America longitudes.) Not only the cross polar cap potentials but also peak potentials on both sides from both models are very similar. The latitudes of both vortices (maximum and minimum potentials) are similar for both models, and the orientation of the ion flow in the polar cap with respect to the noon–midnight meridian is also similar. However, the dawnside cell vortex occurs near 0300 APLT in the new MHS while it occurs near 0600 MLT in HMR89. In fact the exact location (the local time) of the dawnside cell appears dependent on season, as indicated in the new MHS model (and the Weimer96 model as well). This shall be discussed later. For Weimer (1996) model calculations, we assume a solar wind speed of 400 m/s. The model potential in Fig. C.2 is for the month of December when the dawnside vortex tends to center approximately at 0300 MLT; for other seasons, the dawnside cell centers at a later time while potentials differ insignificantly. Again the Weimer model potentials

on both sides and ϕ_{pc} are similar to those given by the new MHS model.

The new Ruohoniemi and Greenwald (2005) model consists of 24 patterns corresponding to three levels of IMF magnitudes each yielding eight patterns for different clock angles in the GSM Y – Z plane. These patterns are generally very similar to ours, however, as noted by Ruohoniemi and Greenwald (2005), their cross polar cap potential drops are significantly lower than those from many other models. It is interesting to note that earlier results for the potential drop based solely on the Millstone ISR were found to be appreciably lower than those from the satellite-based ones (Evans et al., 1980; Oliver et al., 1983). For the new MHS model, however, after a more extensive examination for various conditions against the HMR89 model (for $K_p \leq 3$), we do not seem to observe a significant underestimate of the potentials. This perhaps benefits from combining the Sondrestrom data with Millstone Hill data. The combined radar field of view allows for appropriate determination of the maximum and minimum potentials under various conditions.

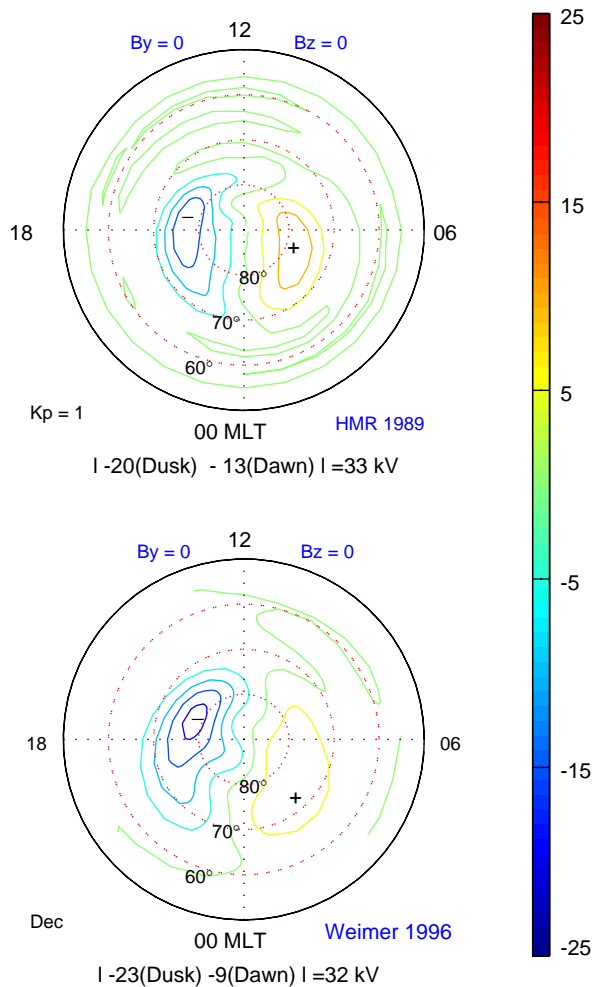


Fig. C.2. Electric potentials for $B_y = B_z = 0$ nT obtained with HMR89 and Weimer96 models. Equipotentials are given at 5 kV interval. Dusk and dawn side potentials as well as the cross polar cap potential ϕ_{pc} are also indicated. For HMR89 model, $K_p = 1$ is assumed which gives $\phi_{pc} = 33$ kV, similar to that shown in Fig. 6. For Weimer96 model, the solar wind speed = 400 m/s for the month of December is assumed.

References

- Alcaydé, D., Caudal, G., Fontanari, J., 1986. Convection electric fields and electrostatic potential over $61 < A < 72$ invariant latitude observed with the European incoherent scatter facility: 1. Initial results. *Journal of Geophysical Research* 91, 233–247.
- Atkinson, G., Hutchison, D., 1978. Effect of the day night ionospheric conductivity gradient on polar cap convection flow. *Journal of Geophysical Research*, 725–729.
- de la Beaujardiére, O., Wickwar, V.B., King, J.H., 1986. Sondrestrom radar observations of the effect of the IMF by component on polar cap convection. In: Kamide, Y., Slavin, J.A. (Eds.), *Solar Wind–Magnetosphere Coupling*. Terra Scientific Publishing Company, Tokyo, pp. 495–505.
- de la Beaujardiére, O., Alcaydé, D., Fontanari, J., Leger, C., 1991. Seasonal dependence of high-latitude electric fields. *Journal of Geophysical Research* 96, 5723–5735.
- Codrescu, M.V., Fuller-Rowell, T.J., Foster, J.C., Holt, J.M., Cariglia, S.J., 2000. Electric field variability associated with the Millstone Hill electric field model. *Journal of Geophysical Research* 105, 5265–5273.
- Crooker, N.U., Rich, F.J., 1993. Lobe-cell convection as a summer phenomenon. *Journal of Geophysical Research* 98, 13403–13407.
- Evans, D.S., Fuller-Rowell, T.J., Maeda, S., Foster, J.C., 1987. Specification of the heat input to the thermosphere from magnetospheric processes using Tiros/NOAA auroral particle observations. *Advances in Astronautical Sciences* 65, 1649–1668.
- Evans, J.V., Holt, J.M., Wand, R.H., 1979. Millstone Hill incoherent scatter observations of auroral convection over $60^\circ \leq A \leq 75^\circ$: 1. Observing and data reduction procedures. *Journal of Geophysical Research* 84, 7059–7074.
- Evans, J.V., Holt, J.M., Oliver, W.L., Wand, R.H., 1980. Millstone Hill incoherent scatter observations of auroral convection over $60^\circ \leq A \leq 75^\circ$. 2. Initial results. *Journal of Geophysical Research* 85, 41–54.
- van Eyken, A.P., Rishbeth, H., Willis, D.M., Cowley, S.W.H., 1984. Initial EISCAT observations of plasma convection at invariant latitudes 70° – 77° . *Journal of Atmospheric and Terrestrial Physics* 46, 635–641.
- Foster, J.C., 1983. An empirical electric field model derived from Chatanika radar data. *Journal of Geophysical Research* 88, 981–987.
- Foster, J.C., 1987. Radar-deduced models of the convection electric field. In: Kamide, Y. (Ed.), *Quantitative Modeling of Magnetosphere–Ionosphere Coupling Processes*. Kyoto Sangyo University, Kyoto, pp. 71–76.
- Foster, J.C., Holt, J.M., Musgrove, R.G., Evans, D.S., 1986a. Solar wind dependencies of high-latitude convection and precipitation. In: Kamide, Y., Slavin, J. (Eds.), *Solar Wind–Magnetosphere Coupling*. Terra Scientific Publishing Company (TERRAPUB), Tokyo, pp. 477–494.
- Foster, J.C., Holt, J.M., Musgrove, R.G., Evans, D.S., 1986b. Ionospheric convection associated with discrete levels of particle precipitation. *Geophysical Research Letters* 13, 656–659.
- Foster, J.C., Turunen, T., Pollari, P., Kohl, H., Wickwar, V.B., 1989. Multi-radar mapping of auroral convection. *Advances in Space Research* 9, (5)19–(5)27.
- Frii-Christensen, E., Kamide, Y., Richmond, A.D., Matsushita, S., 1985. Interplanetary magnetic field control of high-latitude electric fields and currents determined from Greenland magnetometer data. *Journal of Geophysical Research* 90, 1325–1338.
- Fuller-Rowell, T.J., Rees, D., Quegan, S., Moffett, R.J., Codrescu, M.V., Millward, G.H., 1996. A coupled thermosphere–ionosphere CTIM. In: Schunk, R.W. (Ed.), *STEP Handbook of Ionospheric Models*, Scientific Committee on Solar Terrestrial Physics (SCOSTEP). NOAA/NGDC Boulder, Co., pp. 217–238.
- Hairston, M.R., Heelis, R.A., 1990. Model of high-latitude ionospheric convection pattern during southward interplanetary magnetic field using DE 2 data. *Journal of Geophysical Research* 95, 2333–2343.
- Hairston, M.R., Heelis, R.A., 1995. Response time of the polar ionospheric convection pattern to changes in the north-south

- direction of the IMF. *Geophysical Research Letters* 22, 631–634.
- Heelis, R.A., 1984. The effects of interplanetary magnetic field orientation on dayside high-latitude ionospheric convection. *Journal of Geophysical Research* 89, 2872–2880.
- Heelis, R.A., Lowell, J.K., Spiro, R.W., 1982. A model of the high-latitude ionospheric convection pattern. *Journal of Geophysical Research* 87, 6339–6345.
- Heelis, R.A., Foster, J.C., de la Beaujardière, O., Holt, J.M., 1983. Multistation measurements of high-latitude ionospheric convection. *Journal of Geophysical Research* 88, 10111.
- Heppner, J.P., 1977. Empirical models of high latitude electric fields. *Journal of Geophysical Research* 82, 1115–1125.
- Heppner, J.P., Maynard, N.C., 1987. Empirical high-latitude electric field models. *Journal of Geophysical Research* 92, 4467–4489.
- Holt, J.M., van Eyken, A.P., 2000. Plasma convection at high latitudes using the EISCAT VHF and ESR incoherent scatter radars. *Annales Geophysicae* 18, 1088–1096.
- Holt, J.M., Wand, R.H., Evans, J.V., 1984. Millstone Hill measurements on 26 February 1979 during the solar eclipse on formation of a midday F-region trough. *Journal of Atmospheric and Terrestrial Physics* 46, 251.
- Holt, J.M., Evans, J.V., Oliver, W.L., Wand, R.H., 1985. Millstone Hill observations of ionospheric convection. *Physics of Space Plasmas*. Scientific Publishers, Cambridge.
- Holt, J.M., Wand, R.H., Evans, J.V., Oliver, W.L., 1987. Empirical models for the plasma convection at high latitudes from Millstone Hill observations. *Journal of Geophysical Research* 92, 203–212.
- Horwitz, J.L., Doupnik, J.R., Banks, P.M., 1978. Chatanika radar observations of the latitudinal distributions of auroral zone electric fields, conductivities, and currents. *Journal of Geophysical Research* 83, 1463–1481.
- Kamide, Y., Vickrey, J.F., 1983. Relative contribution of ionospheric conductivity and electric field to the auroral electrojets. *Journal of Geophysical Research* 88, 7989–7996.
- Liang, J., Sofko, G.J., Frey, H.U., 2006. Postmidnight convection dynamics during substorm expansion phase. *Journal of Geophysical Research* 111, A04205.
- Liou, K., Newell, P.T., Sibeck, D.G., Meng, C.-I., Brittnacher, M., Parks, G., 2001. Observation of IMF and seasonal effects in the location of auroral substorm onset. *Journal of Geophysical Research* 106, 5799–5810.
- Lu, G., Reiff, P.H., Hairston, M.R., Heelis, R.A., Karty, J.L., 1989. Distribution of convection potential around the polar cap boundary as a function of the interplanetary magnetic field. *Journal of Geophysical Research* 94, 13447–13461.
- Lu, G., Richmond, A.D., Emery, B.A., Reiff, P.H., de la Beaujardière, O., Rich, R.J., Denig, W.F., Kroehl, H.W., Lyons, L.R., Ruohoniemi, J.M., Friis-Christensen, E., Opgenoorth, H., Persson, M.A.L., Lepping, R.P., Rodger, A.S., Hughes, T., McEwin, A., Dennis, S., Morris, R., Burns, G., Tomlinson, L., 1994. Interhemispheric asymmetry of the high-latitude ionospheric convection pattern. *Journal of Geophysical Research* 99, 6491–6510.
- Matsuo, T., Richmond, A.D., Hensel, K., 2003. High-latitude ionospheric electric field variability and electric potential derived from DE-2 plasma drift measurements: dependence on IMF and dipole tilt. *Journal of Geophysical Research* 108, 1005.
- Nopper Jr., R.W., Carovillano, R.L., 1979. On the orientation of the polar cap electric field. *Journal of Geophysical Research*, 6489–6492.
- Oliver, W.L., Holt, J.M., Wand, R.H., Evans, J.V., 1983. Millstone Hill incoherent scatter observations of auroral convection over $60^\circ < A < 75^\circ$. 3. Average patterns vs Kp. *Journal of Geophysical Research* 88, 5505–5516.
- Papitashvili, V.O., Rich, F.J., 2002. High-latitude ionospheric convection models derived from Defense Meteorological Satellite Program ion drift observations and parameterized by the interplanetary magnetic field strength and direction. *Journal of Geophysical Research* 107, 1198.
- Papitashvili, V.O., Belov, B.A., Faermark, D.S., Feldstein, Ya.I., Golyshev, S.A., Gromova, L.I., Levitin, A.E., 1994. Electric potential patterns in the northern and southern polar regions parameterized by the interplanetary magnetic field. *Journal of Geophysical Research* 99, 13251.
- Rich, F.J., Maynard, N.C., 1989. Consequences of using simple analytical functions for the high-latitude convection electric field. *Journal of Geophysical Research* 94, 3687.
- Rich, F.J., Hairston, M., 1994. Large-scale convection patterns observed by DMSP. *Journal of Geophysical Research* 99, 3827–3844.
- Richmond, A.D., Kamide, Y., 1988. Mapping electrodynamic features of the high-latitude ionosphere from localized observations: technique. *Journal of Geophysical Research* 93, 5741–5759.
- Richmond, A.D., Kamide, Y., Ahn, B.-H., Akasofu, S.-I., Alcaydè, D., Blanc, M., de la Beaujardière, O., Evans, D.S., Foster, J.C., Friis-Christensen, E., Fuller-Rowell, T.J., Holt, J.M., Knipp, D., Kroehl, H.W., Lepping, R.P., Pellinen, R.J., Senior, C., Zaitzev, A.N., 1988. Mapping electrodynamic features of the high-latitude ionosphere from localized observations: combined incoherent-scatter radar and magnetometer measurements for January 18–19, 1984. *Journal of Geophysical Research* 93, 5760–6776.
- Ridley, A.J., Lu, G., Clauer, C.R., Papitashvili, V.O., 1998. A statistical study of the ionospheric convection response to changing interplanetary magnetic field conditions using the assimilative mapping of ionospheric electrodynamics technique. *Journal of Geophysical Research* 103, 4023–4039.
- Ruohoniemi, J.M., Greenwald, R.A., 1996. Statistical patterns of high-latitude convection obtained from Goose Bay HF radar observations. *Journal of Geophysical Research* 101, 21743–21763.
- Ruohoniemi, J.M., Greenwald, R.A., 1997. Rates of scattering occurrence in routine HF radar observations during solar cycle maximum. *Radio Science* 32, 1051–1070.
- Ruohoniemi, J.M., Greenwald, R.A., 2005. Dependencies of high-latitude plasma convection: consideration of interplanetary magnetic field, seasonal, and universal time factors in statistical patterns. *Journal of Geophysical Research* 110, A09204.
- Senior, C., Fontaine, D., Caudal, G., Alcaydè, D., Fontanari, J., 1990. Convection electric fields and electrostatic potential over $61 < A < 72$ invariant latitude observed with the European incoherent scatter facility: 2. Statistical results. *Annales Geophysicae* 8, 257–272.
- Smith, M.F., Lockwood, M., 1996. Earth's magnetospheric cusps. *Reviews of Geophysics* 34, 233–260.
- Tanaka, T., 2001. Interplanetary magnetic field B_y and auroral conductance effects on high-latitude ionospheric

- convection patterns. *Journal of Geophysical Research* 106, 24505–24516.
- Weimer, D.R., 1995. Models of high-latitude electric potentials derived with a least error fit spherical harmonic coefficients. *Journal of Geophysical Research* 100, 19595–19607.
- Weimer, D.R., 1996. A flexible IMF dependent model of high-latitude electric potentials having “space weather” applications. *Geophysical Research Letters* 23, 2549–2552.
- Weimer, D.R., 1999. Substorm influence on the ionospheric electric potentials and currents. *Journal of Geophysical Research* 104, 185–197.
- Weimer, D.R., 2001. An improved model of ionospheric electric potentials including substorm perturbations and application to the geospace environment modeling November 24, 1996, event. *Journal of Geophysical Research*, 407–416.
- Wolf, R.A., 1970. Effects of ionospheric conductivity on convective flow of plasma in the magnetosphere. *Journal of Geophysical Research* 75, 4677–4698.
- Yasuhara, F., Greenwald, R., Akasofu, S.-I., 1983. On the rotation of the polar cap potential pattern and associated polar phenomena. *Journal of Geophysical Research* 88, 5773–5777.